

FUSE, STIS, and Keck spectroscopic analysis of the UV-bright star vZ 1128 in M3 (NGC 5272)

P. Chayer,^{1*} W. V. Dixon,¹ A. W. Fullerton,¹ B. Ooghe-Tabanou,^{2,3} and I. N. Reid¹

¹*Space Telescope Science Institute, Baltimore, MD 21218, USA*

²*École Normale Supérieure, Laboratoire de Radio-Astronomie, 28 rue Chomond, 75005 Paris, France*

³*Current address: Sciences Po-Médialab, 84 rue de Grenelle, 75007 Paris, France*

6 June 2021

ABSTRACT

We present a spectral analysis of the UV-bright star vZ 1128 in M3 based on observations with the *Far Ultraviolet Spectroscopic Explorer (FUSE)*, the Space Telescope Imaging Spectrograph (STIS), and the Keck HIRES echelle spectrograph. By fitting the H I, He I, and He II lines in the Keck spectrum with non-LTE H-He models, we obtain $T_{\text{eff}} = 36,600$ K, $\log g = 3.95$, and $\log N(\text{He})/N(\text{H}) = -0.84$. The star's *FUSE* and STIS spectra show photospheric absorption from C, N, O, Al, Si, P, S, Fe, and Ni. No stellar features from elements beyond the iron peak are observed. Both components of the N v $\lambda 1240$ doublet exhibit P Cygni profiles, indicating a weak stellar wind, but no other wind features are seen. The star's photospheric abundances appear to have changed little since it left the red giant branch (RGB). Its C, N, O, Al, Si, Fe, and Ni abundances are consistent with published values for the red-giant stars in M3, and the relative abundances of C, N, and O follow the trends seen on the cluster RGB. In particular, its low C abundance suggests that the star left the asymptotic giant branch before the onset of third dredge-up.

Key words: spectroscopy — stars: abundances — stars: individual: NGC 5272 vZ 1128

1 INTRODUCTION

In the color-magnitude diagrams of globular clusters, UV-bright stars are those objects bluer than the red giant branch and brighter than the horizontal branch. They consist of stars that are evolving to the white dwarf stage, either from the asymptotic giant branch (AGB) or directly from the extreme horizontal branch (EHB). Their atmospheric parameters and abundances should thus provide important constraints on theories of mixing and mass-loss in AGB stars and the formation and evolution of white dwarfs. To study these effects, we have analyzed archival *FUSE*, *HST*/STIS, and Keck HIRES spectra of vZ 1128, the well-known UV-bright star in the globular cluster M3 (NGC 5272).

The star was first catalogued by von Zeipel (1908). It was studied spectroscopically by Strom & Strom (1970), who found it to be a cluster member of late-O spectral type, with an effective temperature $31,500 \text{ K} < T_{\text{eff}} < 35,000 \text{ K}$, a surface gravity $3.9 < \log g < 5.2$, a stellar mass $M > 0.6 M_{\odot}$, and a helium content similar to that of normal Population I stars. The spectrum showed absorption from N,

O, and Si, but its low resolution precluded a detailed abundance analysis. By comparing 11 UV-bright stars in globular clusters with post-HB evolutionary tracks, Strom et al. (1970) concluded that most evolved from HB stars, while the three brightest (including vZ 1128) are post-AGB objects. Garrison & Albert (1986) derived a spectral type of O8p.

The star's high temperature makes it a perfect target for far-ultraviolet spectroscopy. It was observed with the *International Ultraviolet Observer* by de Boer (1985), who derived a temperature $T_{\text{eff}} = 30,000 \pm 2000$ K, a surface gravity $\log g = 4.0$, and a luminosity $\log L/L_{\odot} = 3.10$. Buzzoni et al. (1992) pointed out that these parameters place the star on the post-AGB evolutionary tracks of Schönberner (1983) and concluded that the star is a *bona fide* post-AGB object. Dixon et al. (1994) observed vZ 1128 with the Hopkins Ultraviolet Telescope and derived $T_{\text{eff}} = 35,000 \pm 1000$ K and $\log g = 4.0 \pm 0.25$.

Because vZ 1128 ($l = 42.5$, $b = +78.8$) lies 10 kpc above the Galactic plane along a line of sight with virtually no extinction ($E(B - V) = 0.01$; Harris 1996, 2010 edition), it is often used as a probe of interstellar gas in the Galactic halo (e.g., de Boer & Savage 1984). Both our *FUSE* (Howk et al. 2003) and STIS (Howk et al. 2006) data were originally ob-

* E-mail: chayer@stsci.edu

tained to support studies of the Galactic halo. In § 2 we describe these observations and our reduction of the data. We present our determination of the star’s atmospheric parameters in § 3 and our abundance analysis in § 4. We model the star’s wind features in § 5. We discuss our results in § 6 and summarize our conclusions in § 7.

2 SPECTROSCOPIC OBSERVATIONS

2.1 Keck Spectroscopy

vZ 1128 was observed using the HIRES echelle spectrograph on the Keck I telescope (Table 1). The spectrograph was configured to use the red cross-disperser and a slit with a width of $0''.861$ and a length of $7''.0$. We retrieved the extracted data from the Keck Observatory Archive (KOA). The standard KOA extraction provides one-dimensional spectra that are flat-fielded, bias and background subtracted, and wavelength calibrated. The extracted spectra consist of the relative flux as a function of wavelength and the uncertainty in the flux. The spectrum ranges from 4288 to 6630 Å and is divided into 30 spectral orders that cover 70 Å on average. For wavelengths above 5200 Å, there are gaps between the spectral orders that increase in size from a few Ångstroms to about 25 Å as the wavelength increases. The H I, He I, and He II lines are well contained within one order and do not spread across adjacent orders. The He I $\lambda 5875$ and He II $\lambda 4686$ lines are not used in the spectral analysis, because the He I $\lambda 5875$ line falls in a gap between the spectral orders 23 and 24, and a defect is present in the red wing of the He II $\lambda 4686$ line.

We normalized the individual spectral orders by fitting the continuum with fifth-order polynomials and dividing the continuum by the fits. We paid special attention to the spectral orders that contain the Balmer lines H α , H β , and H γ , because the lines span significant portions of these orders. We fitted the continuum on both sides of the Balmer lines with a fifth-order polynomials, then drew a straight line using only the end-points of the polynomials. The straight lines span the Balmer lines. The end points are 6551 and 6571 Å for H α , 4851 and 4871 Å for H β , and 4329 and 4349 Å for H γ . Figure 1 shows such a fit for H γ . The normalization is carried out by dividing the continuum by the best-fit polynomials and by the straight lines that cover the Balmer lines. Finally, the spectral orders were merged to form a single normalized spectrum.

Table 2 gives the equivalent widths of the Balmer and helium lines, as well as of the N III and O III lines that are observed in the HIRES spectrum. Our equivalent widths are significantly smaller than those measured by Strom & Strom (1970) from a Carnegie image-tube spectrogram of vZ 1128 obtained with the Hale telescope at the Palomar Observatory. The resolution of their spectrogram was roughly 1–2 Å. The equivalent widths that they measured for the He I $\lambda 4388$, He I $\lambda 4471$, and He II $\lambda 4542$ line are 560 mÅ, 1000 mÅ, and 1050 mÅ, respectively. Table 2 shows that our measurements give equivalent widths that are smaller by 42%, 34%, and 63%. Strom & Strom (1970) also measured the equivalent widths of elements other than He. They tentatively identified a few metal lines that they attributed to N, O, and Si, but given the resolution of their observation,

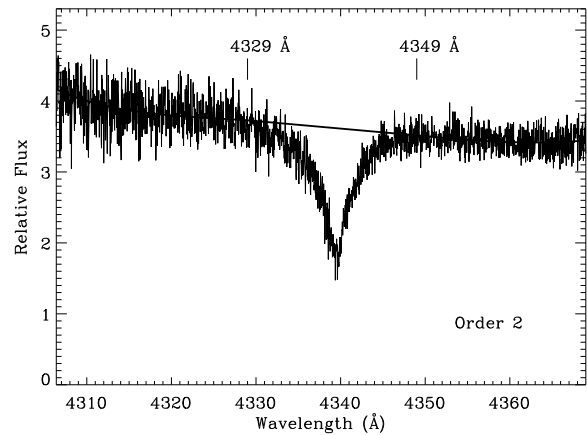


Figure 1. vZ 1128’s Keck HIRES spectral order number 2 showing H γ . The thick curve is the best fit of the continuum.

Table 2. Photospheric lines observed in the HIRES spectrum of vZ 1128.

Ion	λ_{lab} (Å)	$\log gf$	E_l (cm^{-1})	E.W. (mÅ)
H γ	4340.46	−0.447	82259.	2752 ± 50
H β	4861.32	−0.020	82259.	2680 ± 42
H α	6562.80	0.710	82259.	2753 ± 41^a
He I	4387.929	−0.880	193918.391	326.5 ± 12.1
	4437.551	−2.030	171135.000	42.8 ± 6.4
	4471.5	0.052	169087.	664.6 ± 15.3
	4713.2	−0.973	169087.	215.4 ± 7.3
	4921.931	−0.430	171135.000	367.3 ± 13.4
He II	5015.678	−0.820	166277.547	209.2 ± 6.4
	5047.738	−1.600	171135.000	81.0 ± 7.1
	4541.593	−0.223	411477.925	389.3 ± 21.2
	5411.516	0.321	411477.925	524.5 ± 19.8
	6560.088 ^b	0.759	421353.135	...
N III	4510.96	−0.059	287591.5	11.8 ± 2.8
	4514.85	0.221	287706.9	24.3 ± 4.4
	4634.13	−0.086	245665.4	$−30.6 \pm 4.3^c$
	4640.64	0.168	245701.3	$−43.9 \pm 4.6^c$
O III	4867.17	0.341	309849.8	$−12.4 \pm 3.5^c$
	5592.252	−0.337	273081.33	48.4 ± 4.4

^aE.W. includes that of the He II line at 6560.088 Å.

^bLine blended with blue wing of H α .

^cLine in emission.

they acknowledged the possibility of blends. The HIRES spectrum shows that only a handful of N and O lines are detected. The N III $\lambda 4511$ and $\lambda 4515$ lines, and the O III $\lambda 5592$ line are in absorption, while the N III $\lambda 4634$, $\lambda 4641$ and $\lambda 4867$ lines are in emission. A handful of faint features remain unidentified. It is difficult to know whether they are real or not.

2.2 FUSE Spectroscopy

The *Far Ultraviolet Spectroscopic Explorer* (FUSE) consists of four independent spectrographs, two with LiF-coated optics that are sensitive to wavelengths between 990 and 1187 Å, and two with SiC-coated optics that provide reflectiv-

Table 1. Summary of the Keck, *FUSE*, and STIS observations.

Data ID	Date	Grating	$R \equiv \lambda/\Delta\lambda$	Wavelength (Å)	Exp. Time (s)	Instrument
HI.19960604.30960	Jun 4 1996	...	47,800	4300–6700	3000	HIRES
P1014101	Jun 18 2000	...	20,000	905–1187	9151	<i>FUSE</i>
P1014102	Jun 19 2000	...	20,000	905–1187	8248	<i>FUSE</i>
P1014103	Jun 22 2000	...	20,000	905–1187	15610	<i>FUSE</i>
O6F502010	Aug 17 2002	E140M	45,000	1140–1735	1960	STIS
O6F502020	Aug 17 2002	E140M	45,000	1140–1735	10712	STIS
O6F501010	Aug 16 2002	E230M	30,000	1574–2382	1930	STIS
O6F501020	Aug 16 2002	E230M	30,000	1574–2382	8034	STIS
O6F501030	Aug 16 2002	E230M	30,000	2303–3111	2784	STIS

ity to wavelengths below the Lyman limit. The four channels overlap between 990 and 1070 Å. For a complete description of *FUSE*, see Moos et al. (2000) and Sahnou et al. (2000). Observations of vZ 1128 totaling 31.5 ks were obtained through the *FUSE* 30'' × 30'' aperture in 2000 June (Howk et al. 2003). A summary of the *FUSE* observations is presented in Table 1. For this project, the data were reduced using v3.1.3 of CalFUSE, the standard data-reduction pipeline software. (A more recent version of the program, v3.2.0, is described by Dixon et al. 2007.) CalFUSE corrects for a variety of instrumental effects, extracts spectra from each of the four *FUSE* channels, and performs wavelength and flux calibration. The extracted spectra are binned by 0.013 Å. The spectra from each exposure were aligned by cross-correlating on the positions of stellar absorption features and combined into a single spectrum for each channel.

In their analysis of the *FUSE* spectrum of vZ 1128, Howk et al. (2003) determined the radial velocity of the star with respect to the local standard of rest (LSR). Because the zero point of the wavelength scale of individual *FUSE* spectra cannot be determined with accuracy, they compared the H I 21 cm emission line profile from Danly et al. (1992) to the absorption profiles corresponding to the Ar I lines at 1048.220 Å and 1066.660 Å. This allowed them to shift the *FUSE* LiF1A spectrum and the other channels to the LSR. They based their comparison on the assumption that the H I emission, when converted to an absorption-line profile, is similar to the Ar profiles. They showed that the neutral and ionized gas along the line of sight of vZ 1128 has LSR velocities between -70 km s^{-1} and $+30 \text{ km s}^{-1}$. After shifting the *FUSE* spectra to the LSR, Howk et al. measured the velocity of about 10 stellar lines, obtaining an average velocity of $V_{\text{LSR}} = -140 \pm 8 \text{ km s}^{-1}$. The heliocentric radial velocity is then $V_{\text{R}} = V_{\text{LSR}} - V_{\odot} \cos 57^{\circ} = -150.9 \text{ km s}^{-1}$, where $V_{\odot} = +20 \text{ km s}^{-1}$ is the solar velocity, and 57° is the angle on the celestial sphere between the Sun's apex and vZ 1128. This radial velocity is close to the value $V_{\text{R}} = -153 \pm 15 \text{ km s}^{-1}$ measured by Strom & Strom (1970).

Howk et al. (2003) used the *FUSE* spectrum of vZ 1128 to study the interstellar matter along the line of sight to the star. They identified about two dozen interstellar lines from ions such as C II, C III, N I, O I, O VI, Si II, P II, S III, Ar I, Fe II, and Fe III. Fig. 2 shows the *FUSE* spectrum of vZ 1128 and identifies the strongest stellar lines. Their properties are summarized in Table 3. The stellar features are easily identifiable, because their radial velocities are well separated from those of the interstellar lines. Also, with an effective temperature of 36,600 K, the dominant ions in the

photosphere of vZ 1128 are two, three, or four times ionized. Surprisingly, the *FUSE* spectrum of vZ 1128 does not show numerous stellar lines. About three dozen lines corresponding to elements such as He, C, N, O, Si, P, and S are detected. No lines from Fe, iron peak elements, or elements beyond Zn are detected. The equivalent widths of the stellar lines (other than the H and He lines) range from $\sim 10 \text{ mÅ}$ to $\sim 170 \text{ mÅ}$. The strongest of these features are the C III $\lambda 1176$; the N III $\lambda 980$, $\lambda 991$, $\lambda 1006$, and $\lambda 1183$; the N IV $\lambda 923$ and $\lambda 955$; and the S IV $\lambda 1068$ multiplets.

2.3 STIS Spectroscopy

High-resolution STIS echelle observations of vZ 1128 were obtained through the $0'.2 \times 0'.06$ aperture of the Space Telescope Imaging Spectrograph (STIS) in 2002 August (*HST* Proposal 9150; Howk et al. 2006). Observations O6F501020 and O6F502020 employed the E140M grating and the FUV Multi-Anode Microchannel Array (MAMA) detector, and observations O6F501010, O6F501020, and O6F501030 used the E230M grating and the NUV MAMA detector. The STIS observations are summarized in Table 1. The data were retrieved from the Mikulski Archive for Space Telescopes¹ and calibrated using the on-the-fly version (2.15c) of CALSTIS in 2005 June. The design and construction of STIS are described by Woodgate et al. (1998), and information about its on-orbit performance is provided by Kimble et al. (1998). Information about CALSTIS can be found in the *HST STIS Data Handbook* (Bostroem & Proffitt 2011).

The STIS spectra consist of three pass bands that cover a wavelength range from about 1140 Å to 3111 Å. We measured a stellar radial velocity of $-151.8 \pm 3.0 \text{ km s}^{-1}$ by using a dozen stellar lines. This velocity agrees with the one measured by Howk et al. (2003) and Strom & Strom (1970). Unlike the *FUSE* spectra, the STIS spectra show many stellar Fe IV and Fe V lines. Table 3 gives the atomic properties of some of the Fe lines that are observed in the STIS E140M spectrum. These Fe IV and Fe V transitions start from relatively high energy levels, but have large oscillator strengths. Consequently, the lines are not very strong and have equivalent widths ranging from about 10 to 50 mÅ. A handful of faint Ni IV and Ni V lines are also detected. Their equivalent widths range from about 7 to 15 mÅ. No other iron-peak elements nor any heavier elements are detected. On the other

¹ <http://archive.stsci.edu/hst/>

Table 3. Photospheric lines used for measuring the abundances in vZ 1128.

Ion	λ_{lab} (Å)	$\log gf$	E_l (cm^{-1})	E.W. (mÅ)	$\log N(X)/N(\text{H})$	Instrument
C III	1175.665 ^a	0.389	52419.400	594.0 ± 14.0	-5.49 ± 0.09	FUSE
	1175.665 ^a	0.389	52419.400	607.0 ± 14.6	-5.42 ± 0.12	STIS
	1247.383	-0.314	102352.040	65.8 ± 4.3	-5.79 ± 0.09	STIS
	1296.377 ^a	0.537	270013.000	9.4 ± 2.4	-5.66 ± 0.18	STIS
	2297.578	-0.264	102352.040	116.5 ± 6.5	-5.51 ± 0.17	STIS
C IV	1168.933 ^a	0.640	324886.094	69.9 ± 4.8	-5.72 ± 0.13	FUSE
	1168.933 ^a	0.640	324886.094	81.9 ± 6.9	-5.65 ± 0.15	STIS
	1548.195	-0.419	0.000	282.4 ± 10.0	-5.48 ± 0.04	STIS
	1550.772	-0.720	0.000	227.9 ± 8.5		STIS
N III	979.876 ^a	0.153	101027.00	282.3 ± 8.2	-4.42 ± 0.13	FUSE
	989.799	-0.610	0.000	171.5 ± 8.2	-4.42 ± 0.09	FUSE
	991.511	-1.317	174.400	242.0 ± 10.4		FUSE
	991.577	-0.357	174.400			FUSE
	1005.993	-0.807	131004.300	100.8 ± 6.2	-4.63 ± 0.09	FUSE
	1006.036	-1.123	131004.300			FUSE
	1182.971	-0.924	145875.700	113.2 ± 5.9	-4.58 ± 0.12	FUSE
	1183.032	-0.608	145875.700			FUSE
	1184.514	-0.212	145985.800	111.7 ± 5.4		FUSE
	1184.574	-0.915	145985.800			FUSE
	1182.971	-0.924	145875.700	105.5 ± 4.4	-4.45 ± 0.11	STIS
	1183.032	-0.608	145875.700			STIS
	1184.514	-0.212	145985.800	115.0 ± 4.9		STIS
	1184.574	-0.915	145985.800			STIS
	4510.96	-0.059	287591.500	11.8 ± 2.8	-4.49 ± 0.11	HIRES
	4514.85	0.221	287706.900	24.3 ± 4.4		HIRES
	4634.13	-0.086	245665.4	$-30.6 \pm 4.3^{\text{b}}$	-4.39 ± 0.15	HIRES
	4640.64	0.168	245701.3	$-43.9 \pm 4.6^{\text{b}}$		HIRES
	4867.17	0.341	309849.8	$-12.4 \pm 3.5^{\text{b}}$	-4.20 ± 0.10	HIRES
	N IV	921.994	-0.551	67272.300	127.9 ± 10.6	-4.38 ± 0.04
922.519		-0.648	67209.200	162.4 ± 10.7		FUSE
924.284		-0.552	67416.300	164.5 ± 9.4		FUSE
955.334		-0.399	130693.900	213 ± 10.1	-4.35 ± 0.06	FUSE
1036.119		0.778	420058.000	72.5 ± 4.6	-4.53 ± 0.09	FUSE
1036.149		0.618	420049.594			FUSE
1036.196		0.447	420045.813			FUSE
1036.237		-0.285	420049.594			FUSE
1036.239		-0.285	420058.000			FUSE
1036.327		-1.829	420058.000			FUSE
1078.711		0.599	429159.600	22.4 ± 3.5	-4.46 ± 0.17	FUSE
1718.550		-0.289	130693.900	197.0 ± 21.9	-4.43 ± 0.22	STIS
N V		1238.821	-0.505	0.000	81.9 ± 4.5	-6.34 ± 0.10
	1242.804	-0.807	0.000	72.8 ± 4.1		STIS
	1138.535	-0.755	210461.797	35.8 ± 4.0	-4.55 ± 0.11	FUSE
O III	1149.634	-1.080	197087.703	37.9 ± 3.4	-4.37 ± 0.09	FUSE
	1150.884	-0.603	197087.703	52.9 ± 3.7		FUSE
	1153.775	-0.382	197087.703	59.7 ± 4.3		FUSE
	5592.252	-0.337	273081.33	48.4 ± 4.4	-4.62 ± 0.12	HIRES
	1067.768	0.504	419533.906	41.0 ± 4.3	-4.27 ± 0.14	FUSE
O IV	1067.832	0.658	419550.594			FUSE
	1338.615	-0.632	180480.797	68.6 ± 3.4	-4.79 ± 0.13	STIS
	1342.990	-1.333	180724.203	46.5 ± 3.2		STIS
	1343.514	-0.380	180724.203	85.0 ± 3.9		STIS
	1371.296	-0.328	158797.703	37.5 ± 3.3	-4.58 ± 0.16	STIS
Al III	1854.716	0.060	0.000	55.3 ± 8.3	-6.87 ± 0.14	STIS
	1862.790	-0.240	0.000	49.2 ± 12.8		STIS
Si III	1109.940	-0.186	52853.281	9.9 ± 2.2	-5.84 ± 0.09	FUSE
	1109.970	0.294	52853.281			FUSE
	1113.174	-1.356	53115.012	24.1 ± 3.2		FUSE
	1113.204	-0.186	53115.012			FUSE
	1113.230	0.564	53115.012			FUSE
	1298.946	0.443	53115.012	13.9 ± 1.8	-6.17 ± 0.06	STIS

Table 3 – *continued* Photospheric lines used for measuring the abundances in vZ 1128.

Ion	λ_{lab} (Å)	$\log gf$	E_l (cm^{-1})	E.W. (mÅ)	$\log N(X)/N(\text{H})$	Instrument	
Si IV	1066.629 ^a	0.961	160375.000	67.7 ± 4.8	-6.22 ± 0.11	FUSE	
	1128.325	-0.480	71748.641	94.8 ± 4.0	-6.21 ± 0.08	FUSE	
	1128.340	0.470	71748.641			FUSE	
	1393.755	0.030	0.000	184.6 ± 6.0	-5.73 ± 0.05	STIS	
	1402.770	-0.280	0.000	146.1 ± 5.6		STIS	
P IV	950.657	0.270	0.000	46.7 ± 6.3	-8.18 ± 0.26	FUSE	
	1028.094	-0.317	67918.031	18.7 ± 3.5	-7.90 ± 0.10	FUSE	
	1030.514	-0.444	68146.477	37.2 ± 3.5		FUSE	
	1030.515	0.255	68615.172			FUSE	
	1033.112	-0.319	68146.477	18.3 ± 3.5		FUSE	
P V	1035.516	-0.222	68615.172	23.1 ± 3.5		FUSE	
	1117.977	-0.010	0.000	82.9 ± 4.1	-8.52 ± 0.12	FUSE	
	1128.008	-0.320	0.000	77.2 ± 3.8		FUSE	
S IV	1062.678	-1.089	0.000	72.8 ± 4.2	-6.61 ± 0.09	FUSE	
	1072.996	-0.829	951.100	70.8 ± 3.5		FUSE	
	1073.528	-1.789	951.100	45.2 ± 3.1		FUSE	
	1098.917	-0.607	94150.398	43.8 ± 4.0	-6.33 ± 0.11	FUSE	
	1099.472	-0.799	94103.102	34.8 ± 4.1		FUSE	
S V	1122.042	0.094	234956.000	41.3 ± 4.1	-6.19 ± 0.17	FUSE	
	1128.667	-0.066	234947.094	23.3 ± 2.6		FUSE	
	1128.776	-0.968	234956.000	13.5 ± 2.1		FUSE	
	1501.760	-0.504	127150.703	71.2 ± 4.4	-6.70 ± 0.16	STIS	
S VI	944.523	-0.350	0.0	70.0 ± 5.3	-6.06 ± 0.16	FUSE	
Fe V	1373.589	0.312	187719.000	22.8 ± 2.6	-6.26 ± 0.15	STIS	
	1373.679	0.188	187157.500	9.9 ± 1.9		STIS	
	1376.337	0.439	188395.297	26.8 ± 2.9		STIS	
	1376.451	0.049	186725.500	16.4 ± 2.7		STIS	
	1378.561	0.430	205536.406	19.6 ± 3.0		STIS	
Fe V	1459.769	0.222	213534.094	38.3 ± 4.1	-6.64 ± 0.16	STIS	
Fe IV	1462.586	-0.761	190811.797	8.2 ± 2.5		STIS	
Fe V	1462.636	0.041	186433.594	15.0 ± 2.5		STIS	
Fe IV	1464.695	0.158	190318.344	18.2 ± 3.5		STIS	
Fe V	1465.380	-0.260	187157.500	15.4 ± 3.1		STIS	
	1465.401	0.304	221305.203			STIS	
	1468.998	0.474	217122.500	21.7 ± 3.4		STIS	
	1472.095	0.396	216860.406	14.6 ± 3.3		STIS	
	1472.511	0.312	216779.094	10.1 ± 3.0		STIS	
	Fe IV	1531.223	0.051	158738.688	18.1 ± 3.6	-5.97 ± 0.15	STIS
	1532.630	-0.129	128541.852	19.8 ± 4.7		STIS	
	1532.903	0.434	168566.438	18.6 ± 4.5		STIS	
1533.267	0.177	159010.391	20.6 ± 4.4		STIS		
1533.869	-0.004	128191.539	47.1 ± 5.4		STIS		
1542.155	0.045	128541.852	20.2 ± 4.7		STIS		
1542.698	0.360	128967.672	37.2 ± 4.6		STIS		
1544.486	0.453	168526.375	20.0 ± 4.2		STIS		
1546.404	-0.318	127929.117	22.8 ± 4.7		STIS		
Ni IV	1398.193	0.584	110410.602	14.5 ± 2.6	-7.87 ± 0.12	STIS	
	1411.451	0.448	111195.797	13.7 ± 2.9	-7.73 ± 0.11	STIS	
Ni V	1244.174	0.443	164525.906	10.6 ± 3.9	-6.95 ± 0.15	STIS	
	1264.501	0.320	164525.906	7.6 ± 2.1	-7.19 ± 0.23	STIS	

^aMultiplet.^bLine in emission.

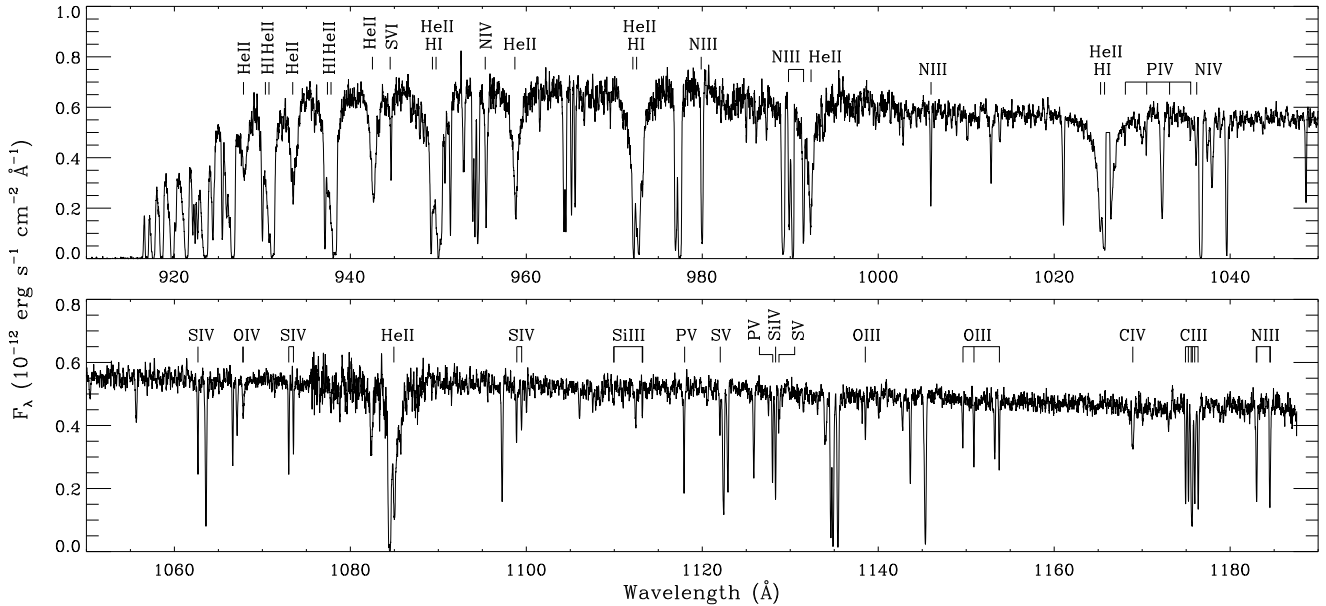


Figure 2. *FUSE* spectrum of vZ 1128. This spectrum was obtained by merging the segments SiC1B, LiF1A, SiC2B, LiF2A, and LiF1B. The strongest photospheric lines are identified above the spectrum. Most unmarked absorption lines are interstellar lines. Their identification is presented in Fig. 2 of Howk et al. (2003), who analyzed the line of sight toward vZ 1128.

hand, several stellar lines coming from light elements are detected. The resonance lines of the C IV $\lambda 1550$ doublet, the N V $\lambda 1240$ doublet, the Al III $\lambda 1857$ doublet, the Si III $\lambda 1206$ line, and the Si IV $\lambda 1397$ doublet are observed. A handful of lines starting from energy levels above the ground state are also detected. For instance, the C III $\lambda 1247$ and $\lambda 2297$ lines, the O IV $\lambda 1340$ triplet, the O V $\lambda 1371$ line, and the S V $\lambda 1501$ line are observed with equivalent widths that vary from ~ 45 mÅ to 85 mÅ. Table 3 summarizes the properties of the lines observed in the STIS spectra.

The STIS E230M data show the He II series for transitions from the lower energy level $n = 3$ to the upper energy levels $n = 6$ through 18. In fact, because the wavelength range of the E230M O6F501020 and O6F501030 datasets covers the region between 1574 Å and 3111 Å, only the transitions $n = 3 \rightarrow 4$ and 5 are missing. These two transitions correspond to the $\lambda 4686$ and $\lambda 3203$ lines. Fig. 3 shows the portions of the STIS E230M spectrum where the He II series is visible. The lower panel shows the He II $\lambda 2733$ and $\lambda 2511$ lines that correspond to the transitions $n = 3 \rightarrow 6$ and 7. The upper panel shows the remaining He II lines, corresponding to the transitions $n = 3 \rightarrow 8$ through 18.

3 DETERMINATION OF ATMOSPHERIC PARAMETERS

By comparing the Keck HIRES spectrum of vZ 1128 to a grid of stellar atmosphere models, and by using a chi-square method to find the best model, we can determine the effective temperature, gravity, and He abundance of the star. We computed a grid of non-local thermodynamic equilibrium (non-LTE) stellar atmosphere models using the program

TLUSTY (Hubeny & Lanz 1995). The models are composed solely of H and He. The atomic models for H, He I, and He II are similar to those that Lanz & Hubeny (2003) used for computing their grid of O-type stars. Our grid of models covers an effective temperature range $T_{\text{eff}} = 26,000$ to 42,000 K in steps of 2000 K, a gravity range $\log g = 3.6$ to 4.8 in steps of 0.2 dex, and a He abundance range $\log N(\text{He})/N(\text{H}) = 0.0$ to -2.0 in steps of 0.5 dex. From that grid of stellar atmosphere models, we computed a grid of synthetic spectra using the program SYNSPEC (I. Hubeny & T. Lanz, private communication). The synthetic spectra cover a wavelength range of 3500 to 6800 Å. The synthetic spectra were convolved with a Gaussian with a FWHM of 0.1 Å and were normalized to replicate the Keck HIRES spectrum. We used the IDL function CURVEFIT to fit the synthetic spectra to the observed Balmer and He lines with the effective temperature, gravity, and He abundance as free parameters.

Fig. 4 shows our best fits to the Balmer and He lines that are observed in the HIRES spectrum. Table 2 gives the atomic parameters and equivalent widths of these lines. The best fit yields an effective temperature $T_{\text{eff}} = 36,600 \pm 400$ K, a gravity $\log g = 3.95 \pm 0.10$, and a He abundance $\log N(\text{He})/N(\text{H}) = -0.84 \pm 0.03$. The uncertainties of the atmospheric parameters are from the quality of the fit and the error associated with our experiments regarding the normalization of the HIRES spectrum. By slightly changing the parameters of the normalization, we obtained slightly different atmospheric parameters. This source of error is incorporated into the uncertainties cited above. Fig. 4 shows that the fit is very good in general. The fit of $H\alpha$ shows some small discrepancies in the core of the line and just next to the He II $\lambda 6560$ line in the blue wing of $H\alpha$. The fits of the $H\alpha$ wings and the He II $\lambda 6560$ line are quite good though.

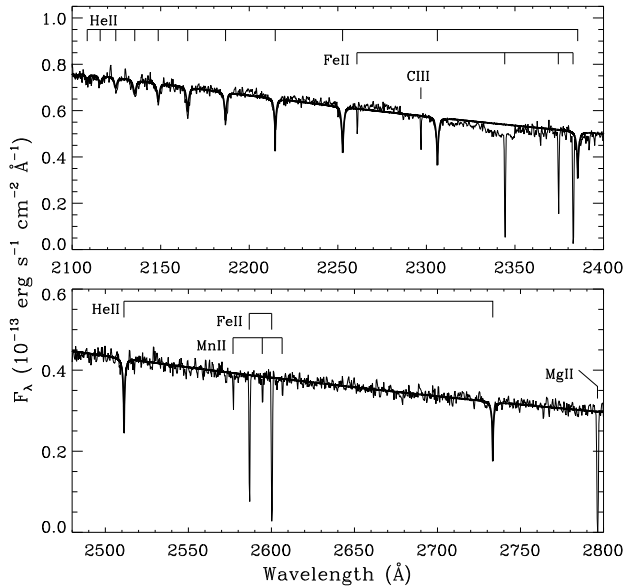


Figure 3. He II line series corresponding to the transitions $n = 3 \rightarrow 6$ up to 18 observed in the STIS E230M spectrum of vZ 1128. The bold curve is a model with $T_{\text{eff}} = 36,600$ K, $\log g = 3.95$, and $\log N(\text{He})/N(\text{H}) = -0.84$ that is scaled to match the flux level of the STIS observation. The Mg II, Mn II, and Fe II absorption features are interstellar lines, while the C III feature is a stellar line.

The model matches H β over the whole line profile, while it shows some discrepancies close to the core of H γ . This discrepancy could indicate that the normalization of the HIRES spectrum around H γ is not as good as the normalization of H α and H β . The forbidden component of the He I $\lambda 4471$ line is well reproduced by the model, but the computed forbidden component of the He I $\lambda 4922$ line is slightly too strong to account for the observation. The kink in the blue wing of the He I $\lambda 4388$ line is caused by its forbidden component. There is a feature in the red wing of the He II $\lambda 5412$ line that is not accounted for, and the computed line profile of the He II $\lambda 4542$ line seems slightly too strong. This could indicate, however, that the normalization of the observed He II $\lambda 4542$ line is not perfect.

4 ABUNDANCE ANALYSIS

4.1 Technique

The abundance of an element is measured by comparing its observed lines to a set of synthetic spectra that are computed for different abundances. We computed grids of non-LTE atmosphere models by adopting the atmospheric parameters derived in § 3, $T_{\text{eff}} = 36,600 \pm 400$ K, $\log g = 3.95 \pm 0.10$, and $\log N(\text{He})/N(\text{H}) = -0.84 \pm 0.03$, and by considering several chemical compositions of five elements at a time. The different compositions that we considered consist of H+He+N+O+X, where X is either C, Al, Si, P, S, or Fe. The models were computed with $\log N(\text{N})/N(\text{H}) = -4.4$ and $\log N(\text{O})/N(\text{H}) = -4.5$, and by considering 15 values of the

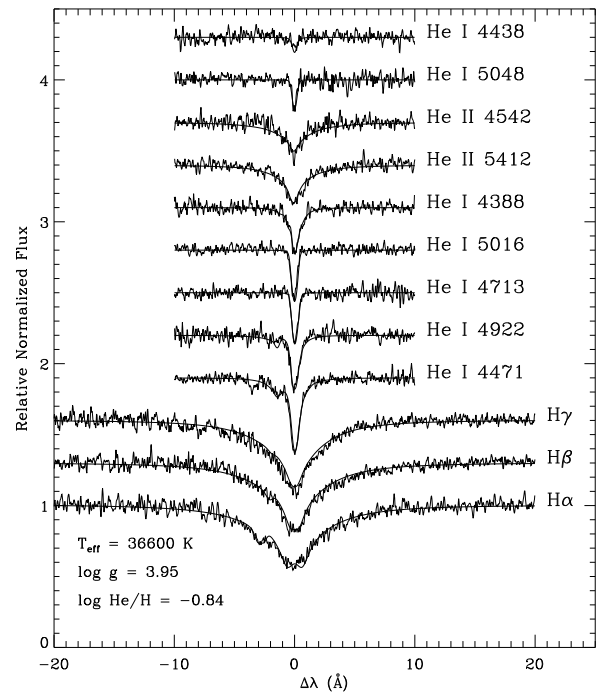


Figure 4. Best-fit model plotted over the Balmer, He I, and He II lines observed in the Keck HIRES spectrum of vZ 1128. The faint absorption feature in the blue wing of H α is the He II $\lambda 6560$ line. The He I $\lambda 5875$ line is not detected in the HIRES spectrum, because the line is located in a gap between two spectral orders. The He II $\lambda 4686$ line is not shown, because the line is corrupted by an artifact and is not usable by the fitting procedure.

abundances $\log N(\text{X})/N(\text{H}) = -4.0$ to -9.2 , in steps of 0.4 dex. The N and O abundances were determined by considering models with a chemical composition of H+He+N+O. These two elements were included in all model calculations because they are the most abundant metals in the stellar photosphere.

Using the non-LTE stellar atmosphere models, we computed synthetic spectra for each abundance and for all the stellar lines observed in the *FUSE*, STIS, and Keck spectra. The resolution of the synthetic spectra was adjusted to match the resolution of the observed spectra. We used the programs TLUSTY and SYNSPEC to compute the non-LTE stellar atmosphere models and synthetic spectra. In order to take into account the uncertainties of the atmospheric parameters, we also computed stellar atmosphere models that include the uncertainties of the effective temperature and gravity ($\Delta T_{\text{eff}} = 400$ K and $\Delta \log g = 0.10$ dex), and repeated the calculations by using the new sets of atmospheric parameters: $T_{\text{eff}} = 37,000$ K and $\log g = 3.95$; $T_{\text{eff}} = 36,600$ K and $\log g = 4.05$.

We use a chi-square minimization method to fit each line or multiplet individually. This method determines the best match between the synthetic spectra and the observations, and estimates the abundance and its uncertainty. We first normalize both the observed and theoretical absorption lines. The observed lines are normalized by dividing the spectrum by a low-order polynomial that fits the continuum on both sides of the lines of interest. The synthetic spectra

are divided by the theoretical continuum computed by the program SYNSPEC. We then shift the observed spectrum to the laboratory rest frame and select the portion of the spectrum that includes the lines of interest for a given element. We use the IDL function CURVEFIT to fit the synthetic spectra to the observed lines with the abundance as a free parameter. Fig. 5 (top row) shows such fits for three absorption lines observed with three different instrument setups. The Si IV $\lambda 1066$ line is observed with the *FUSE* LiF1A segment, the C III $\lambda 1247$ line is observed with the STIS E140M grating using the NUV MAMA detector, and the C III $\lambda 2297$ line is observed with the STIS E230M grating using the FUV MAMA detector.

4.2 Additional Broadening

At first sight, the match between the synthetic spectra and the observed lines plotted in Fig. 5 (top row) seems quite good, but the cores of the models are systematically too deep and the wings are too narrow. A better match between the observed data and model is obtained by considering an additional source of broadening, such as the projected stellar rotational velocity $v \sin i$ or the microturbulent velocity ξ . For example, Fig. 5 (middle row) shows the best fits to the same lines, but considering both the abundance and the rotational velocity as free parameters. By eye we can see that the quality of the fits has improved. Though the changes are small, the cores and wings of the lines better match the observations. The $\Delta\chi^2$ values displayed in Fig. 5 (middle row) indicate that χ^2 is significantly lower when we vary both the abundance and rotational velocity than when we vary the abundance alone. The average value of $v \sin i$ for these three measurements is 14.3 km s^{-1} . The better fits accommodate slightly higher abundances.

Microturbulence is another possible source of line broadening. The microturbulent velocity ξ is usually introduced to remove the variation of the abundance as a function of the equivalent width for lines of a given ion. Unfortunately, given the small number of absorption lines observed in the FUV and visible spectra of vZ 1128, we cannot independently determine the microturbulent velocity ξ by using this method. We can estimate the effect of microturbulence on the shape of the metal lines, though, and see whether it is a plausible explanation for the additional broadening. Fig. 5 (bottom row) shows our best fits when considering the abundance and the microturbulent velocity as free parameters. The quality of the fits is as good as those for which we considered the abundance and the projected rotational velocity as free parameters. This is illustrated by the negative $\Delta\chi^2$ values, which indicate that these fits yield lower χ^2 than the fits illustrated in the top row of Fig. 5. The average value of ξ for these three measurements is 7.9 km s^{-1} . Unlike rotation, the inclusion of microturbulence in the model decreases the derived abundance. The lines in question are saturated, so increasing ξ broadens them, reducing the saturation and increasing the absorption for a fixed abundance.

Based on spectroscopic analysis alone, we face the dilemma of choosing the source of the line broadening. As discussed above, we cannot measure independently the microturbulent velocity by comparing the equivalent widths and abundances of absorption lines for a given ion. Neither do we have independent information on the projected rota-

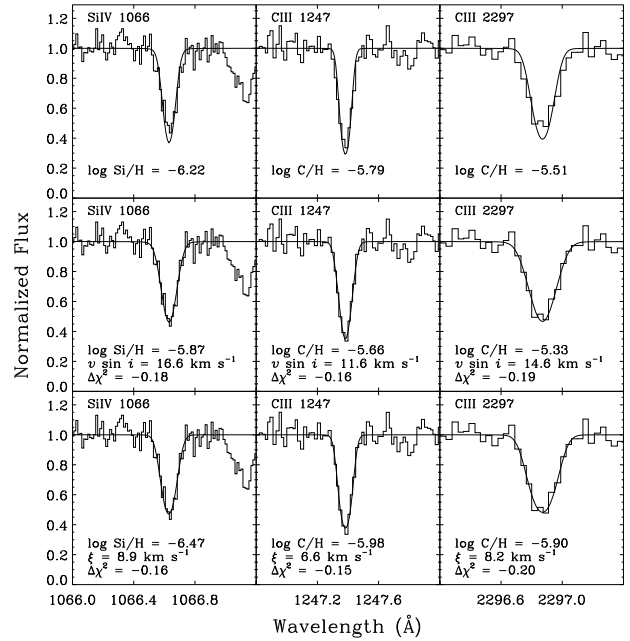


Figure 5. Best fits to the Si IV $\lambda 1066$ line, the C III $\lambda 1247$ line, and the C III $\lambda 2297$ line when considering *i*) the abundance as the only free parameter (*top row*); *ii*) the abundance and the projected rotational velocity $v \sin i$ as free parameters (*middle row*); and *iii*) the abundance and the microturbulent velocity ξ as free parameters (*bottom row*).

tional velocity of the star. Given that both sources of line broadening yield practically identical results, we cannot rule out one or the other solely on the basis of the spectral observations. Both sources of line broadening could be present simultaneously in different degrees. Consequently, instead of choosing one particular source of line broadening, we have adopted the approach of considering 1) the abundance as the only free parameter; 2) the abundance and the stellar projected rotational velocity $v \sin i$ as free parameters; and 3) the abundance and the microturbulent velocity ξ as free parameters. This approach allows us to move forward with our abundance analysis. It also shows us the effects of including either the stellar rotation or the microturbulent velocity on the determination of the abundances for all species observed in the atmosphere of vZ 1128.

4.3 Results

Table 3 lists the atomic and observed properties of the stellar lines that we selected to measure the abundances. The abundances quoted in the table were measured by assuming no additional line broadening. The table shows the abundances for individual transitions and ions. The uncertainties of the abundances include the quality of the fit, the oscillator strength uncertainty, and the atmospheric parameter uncertainties (ΔT_{eff} and $\Delta \log g$). The oscillator strength uncertainties are based on the National Institute of Standard and Technology website.² The different contributions to the uncertainties are combined in quadrature. Table 4 presents

² http://physics.nist.gov/PhysRefData/ASD/lines_form.html

Table 4. Comparison between the abundances observed in vZ 1128 and those in HB and RGB stars in M 3.

Elements	vZ 1128			Microturbulence		M 3	Ref.
	Stellar Rotation		$v \sin i$ (km s ⁻¹)	$\log N(X)/N(H)$	ξ (km s ⁻¹)	$\log N(X)/N(H)$	
	$\log N(X)/N(H)$	$\log N(X)/N(H)$					
He	-0.84 ± 0.03	-1.50 ± 0.39	1
C	-5.59 ± 0.13	-5.43 ± 0.15	13.1 ± 1.4	-6.13 ± 0.23	7.8 ± 1.0	-5.79 ± 0.15	2
N	-4.44 ± 0.15	-4.45 ± 0.11	15.6 ± 3.4	-4.73 ± 0.15	6.2 ± 2.7	-4.69 ± 0.28	2
O	-4.53 ± 0.19	-4.41 ± 0.23	14.1 ± 1.4	-4.85 ± 0.42	6.9 ± 0.4	-4.37 ± 0.15	3
Al	-6.87 ± 0.14	-6.54 ± 0.14	14.7 ± 3.1	-6.99 ± 0.14	8.8 ± 2.3	-6.60 ± 0.36	3
Si	-6.01 ± 0.22	-5.92 ± 0.09	15.4 ± 1.6	-6.75 ± 0.40	8.3 ± 1.0	-5.73 ± 0.06	3
P	-8.20 ± 0.31	-8.18 ± 0.12	13.4 ± 1.1	-9.50 ± 0.12	7.3 ± 0.8
S	-6.38 ± 0.27	-5.97 ± 0.16	17.3 ± 1.5	-6.96 ± 0.38	9.5 ± 3.2
Fe	-6.29 ± 0.34	-5.91 ± 0.19	12.7 ± 1.5	-6.29 ± 0.32	8.4 ± 0.9	-6.06 ± 0.06	3
Ni	-7.43 ± 0.44	-7.38 ± 0.04	3

REFERENCES. — (1) Behr (2003); (2) Smith et al. (1996); (3) Sneden et al. (2004).

the results of our abundance analysis. The second column gives the abundances that are measured without any additional broadening; the third and fourth columns give the parameters that are measured when both the abundance and projected rotational velocity are considered; the fifth and sixth columns give the parameters that are measured when both the abundance and microturbulent velocity are considered. The abundances and velocities are the averages of individual transitions. The uncertainties are the standard deviation of the measurements. Before discussing the result of our abundance analysis, we will report on our analysis of the individual elements.

4.3.1 Helium

As reported earlier, the best fit to the HIRES spectrum yields a He abundance of $\log N(\text{He})/N(\text{H}) = -0.84 \pm 0.03$. Fig. 4 shows the He I and He II lines that were included in the fit. This He abundance is consistent with the strength of the He II line series $n = 3 \rightarrow 6$ through 18 that is observed in the STIS spectrum (Fig. 3). It is also consistent with the strength of the He II line series $n = 2 \rightarrow 3$ through 15 that is observed in the FUSE and STIS spectra.

4.3.2 Carbon

C III and C IV lines are observed in both FUSE and STIS spectra. No C II lines are detected. The resonance C III line at 977.020 Å is not listed in Table 3, because it is blended with the strong interstellar medium absorptions of O I and C III. The C IV lines at 1548.195 and 1550.772 Å are the strongest carbon lines. Although the red wings of the stellar doublet are blended with the interstellar medium absorptions, the separation between both components is wide enough to allow a measurement of the carbon abundance. The individual components of the C III $\lambda 1175$ sextuplet have an equivalent width of about 100 mÅ. The detection of the C III $\lambda 1175$ sextuplet in both FUSE and STIS E140m spectra offers a way to verify that the additional broadening is not caused by unaccounted instrument motions. By using the sextuplet observed in both instruments, we measured

almost identical C abundances, $v \sin i$, and microturbulent velocities ξ .

4.3.3 Nitrogen

Nitrogen lines are detected in the FUSE, STIS, and HIRES spectra. Three ionisation stages are observed: N III, N IV, and N V. All lines are in absorption except for three N III emission lines that are observed in the HIRES spectrum, and the P Cygni profiles in the N V $\lambda 1240$ doublet. We will discuss the P Cygni profiles in more details in § 5. By looking at Table 3, it is interesting to note that the photospheric absorptions in the N V $\lambda 1240$ doublet yield a significantly lower abundance than the ones corresponding to the other N lines. This lower abundance is likely due to the filling of the absorption lines by scattered light that comes from the stellar wind. The abundance of the N V doublet is not included in the average abundance given in Table 4.

To compute the N III emission lines, we first used the N III model atom that Lanz & Hubeny (2003, 2007) built to compute their grids of non-LTE line-blanketed model atmospheres of B and O stars. The model atom contains 24 individual energy levels and considers 184 allowed transitions. Although our models predicted the appearance of the N III emission lines $\lambda 4634$ and $\lambda 4640$, they failed to produce the emission line $\lambda 4867$. In fact, the models produced the $\lambda 4867$ line in absorption. We therefore opted for a more elaborate N III model atom, which we retrieved from the TLUSTY website³. The model consists of 40 individual energy levels and 403 allowed transitions. It includes the $\lambda 4867$ $3p \ ^4D - 3d \ ^4F$ transition explicitly. Using this model atom, we recomputed a grid of stellar models. The new models produced the N III $\lambda 4634$, $\lambda 4640$, and $\lambda 4867$ lines in emission. All of the N abundances given in Table 3 are measured using the more sophisticated N III model atom.

The N IV $\lambda 1036$ and $\lambda 1078$ lines also required additional effort. The N abundances initially derived from these features were factors of 10 and 3 larger (respectively) than the mean. We traced this discrepancy to our choice of oscillator strengths. We had used the atomic line lists that

³ <http://nova.astro.umd.edu/>

are provided on the TLUSTY website. These line lists were extracted from the compilation of Kurucz & Bell (1995)⁴ and updated with newer oscillator strengths and several new lines from the NIST Atomic Spectra Database⁵. Although many N IV lines have been updated, the $\lambda 1036$ and $\lambda 1078$ oscillator strengths definitely underestimated the strength of the observed lines. We replaced these oscillator strengths with the larger values found in Peter van Hoof’s Atomic Line List website⁶, which were compiled from the Opacity Project (Tully et al. 1990). The oscillator strengths agree with those published by Allard et al. (1990, 1991), who compiled N IV atomic data from several sources that include data from the Opacity Project. The $\lambda 1078$ oscillator strength does not agree, however, with the value compiled by Wiese et al. (1996), who report a lower value ($\log gf = 0.175$). Unfortunately, the N IV $\lambda 1036$ oscillator strength is not listed in the extensive compilation of Wiese et al. (1996). Our observations favor the oscillator strengths that are reported in the compilations of Peter van Hoof and Allard et al. (1990, 1991).

4.3.4 Oxygen

Like nitrogen, oxygen is observed in three ionisation stages in the FUV, UV, and optical wavelength ranges. All lines are observed in absorption. Although the abundances of the O IV lines show a relatively large dispersion, the average O IV abundance is consistent with the O III and O V abundances.

4.3.5 Aluminum

The Al abundance is determined by analysing the photospheric Al III $\lambda 1854$ and 1862 resonance doublet. Because the photospheric doublet is well separated from the interstellar medium component, its abundance is well determined. No other photospheric Al lines are detected.

4.3.6 Silicon

A handful of Si III and Si IV transitions are observed. An absorption feature is observed at the wavelength corresponding to the photospheric Si III $\lambda 1206$ resonance line, but the feature seems to be blended. Because the nature of this additional opacity is unclear, the line is not included in the calculation of the abundance. The strong $\lambda 1206$ interstellar medium feature is present at longer wavelengths. The Si III $\lambda 1298$ line is the only line of the sextuplet that is observed.

4.3.7 Sulfur

Only one component of the S VI resonance doublet is detected, because the $\lambda 933$ line is blended with the He II line ($n = 2 \rightarrow 13$).

4.3.8 Iron

We determined the Fe abundance by fitting spectral regions that are dominated by only Fe lines. We selected three regions that include i) only Fe IV lines, ii) only Fe V lines, and iii) a mix of Fe IV and Fe V lines. Table 3 identifies the lines that are included in these regions. It is worth noting that the Fe abundance that is determined when considering microturbulence is the same as the abundance derived without additional source of line broadening. Table 4 shows that the Fe abundances are equal, although the abundances of the other elements are not. This illustrates the fact that the Fe lines are not saturated.

4.3.9 Nickel

Only a few faint Ni IV and Ni V lines are detected. In fact, these lines are the ones that are expected to be observed, because they correspond to transitions with large oscillator strengths that start from low-lying energy levels. No information on the projected stellar rotational velocity or microturbulent velocity could be obtained from these lines, because they are too faint.

5 MASS LOSS

The FUV spectra of many hot post-AGB stars (particularly the central stars of planetary nebulae) exhibit wind features from a variety of species (e.g., Guerrero & De Marco 2013). The spectrum of vZ 1128 exhibits P Cygni profiles in the N V $\lambda 1240$ doublet. Both components show broad blue-shifted absorption and faint red-shifted emission relative to the star’s photospheric lines. The emission seems to be attenuated by interstellar N V absorption.

Fig. 6 compares the N V $\lambda 1240$ lines to the resonance lines of Si IV $\lambda 1397$, C IV $\lambda 1550$, Al III $\lambda 1857$, and O VI $\lambda 1034$ observed in the STIS and *FUSE* spectra. For all five species, the photospheric and interstellar absorption features are aligned in velocity (with the exception of photospheric O VI absorption, which is absent in this star). The N V P Cygni absorption troughs span heliocentric velocities between about -700 km s^{-1} and -150 km s^{-1} and reach depths of $\sim 30\%$ to 40% below the continuum. The continuum for the other resonance lines is flat in this velocity range; no broad absorption is observed. The N V $\lambda 1240$ lines are the only spectral features in either the *FUSE* or STIS bands that exhibit P Cygni profiles.

To constrain the properties of the wind, we fit a simple model to the N V doublet using the line-fitting routines of D. Massa, which combine the Sobolev with exact integration (SEI) algorithm described by Lamers et al. (1987) with the wind optical depth law introduced by Massa, Prinja & Fullerton (1995). This approach uses the standard “beta law” parameterization of the velocity, which has the form

$$w(x) = w_0 + (1 - w_0)(1 - 1/x)^\beta, \quad (1)$$

where $w(x) = v(x)/v_\infty$, $x = r/R_*$, R_* is the stellar radius, and w_0 is the initial velocity at the base of the wind. (In this formalism, all wind velocities are expressed as a fraction of the terminal velocity v_∞ .) The parameter β , which defines

⁴ <http://kurucz.harvard.edu/linelists.html>

⁵ <http://www.nist.gov/pml/data/asd.cfm>

⁶ <http://www.pa.uky.edu/~peter/atomic/>

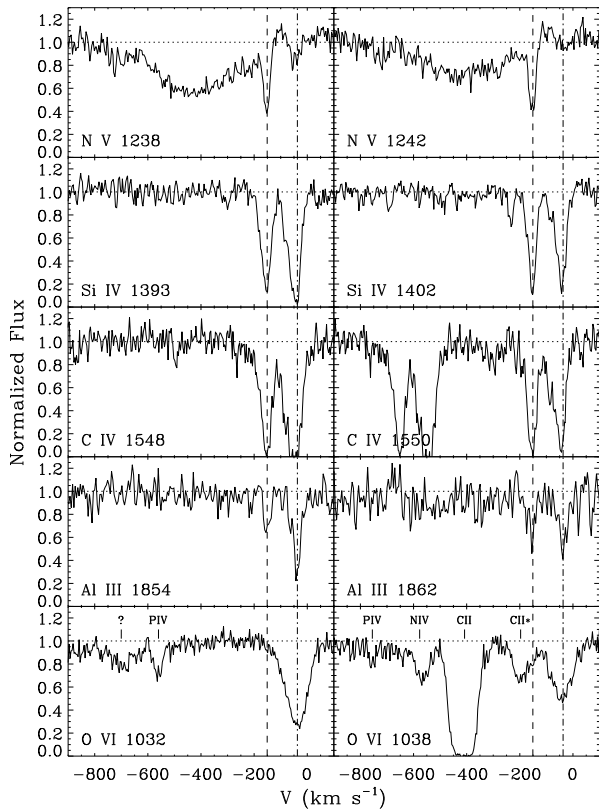


Figure 6. Normalized profiles of the resonance doublets observed in the STIS and *FUSE* spectra of vZ 1128 in the heliocentric frame. The dotted line corresponds to the normalized continuum. The vertical dashed line indicates the radial velocity of vZ 1128 ($V_R = -150.9 \text{ km s}^{-1}$). The vertical dot-dashed line indicates the central velocity of the interstellar O VI lines, $V_R = -37.2 \text{ km s}^{-1}$, given in Howk et al. (2003).

the spatial velocity gradient in the wind, is constrained by the shape of the emission component of the P-Cygni profile. Other inputs to the code are the turbulent velocity w_D , which simulates macroscopic velocity fields in the wind by smoothing the wind profile; the input photospheric spectrum; and $\tau_r(w)$, the radial component of the optical depth of the absorbing species as a function of the wind velocity.

Once β and v_∞ are determined, the resonance lines are fit by adjusting w_D and the elements of $\tau_r(w)$. The photospheric spectrum is modeled with a flat continuum. The N v profile is well fit by the parameters $v_\infty = 380 \text{ km s}^{-1}$, $w_0 = 0.01$, $\beta = 0.5$, and $w_D = 0.2$. The optical depth is roughly constant throughout the wind, with $\tau_r \sim 0.8$. Our best-fit model is presented in Fig. 7. A complete explanation of this technique, its applicability, and its limitations may be found in Massa et al. (2003).

From the stellar abundances and our wind model, we can estimate $\dot{M}q(w)$, the product of the stellar mass-loss rate and the fraction of nitrogen in the form of N^{+4} as a function of velocity in the wind. Averaging over the velocity range $0.2 < w < 0.75$, where our fit to τ_r is most reliable, we find that $\langle \dot{M}q \rangle = 10^{-11} M_\odot \text{ yr}^{-1}$. Our stellar model predicts that $q = 0.1$ at the outer limit of the photosphere. If q is constant throughout the wind, then $\dot{M} = 10^{-10} M_\odot$

Table 5. Optical Depths of Possible Wind Features

Parameter	N v	Si iv	C iv
$q(r = R_*)$	0.10	< 0.01	0.04
$\log A/H$	-4.44	-6.03	-5.59
f	0.156	0.513	0.190
$\lambda (\text{\AA})$	1238.821	1393.755	1548.202
$\tau_r/\tau_r(\text{N v})$	1.00	< 0.01	0.05

yr^{-1} . Pauldrach et al. (1988) compute terminal velocities and mass-loss rates for the winds of Pop. I central stars of PNe. For a star with $M = 0.546 M_\odot$ (§6.4) and $T_{\text{eff}} = 36,000 \text{ K}$, their models predict $v_\infty \sim 1700 \text{ km s}^{-1}$ and $\dot{M} \sim 1.5 \times 10^{-9} M_\odot \text{ yr}^{-1}$. It is likely that models assuming Pop. II abundances would predict lower values for both parameters, since such stars have fewer opacity sources to drive the wind. It is also likely that $q(w)$ is not constant, but falls with increasing velocity (and thus distance from the star), so that our N v profile does not probe the highest velocities achieved by the wind.

In the photosphere of vZ 1128, the abundances of nitrogen and oxygen exceed those of the other metals by more than an order of magnitude. The star is too cool to exhibit significant O VI absorption. Should we expect wind features from other species? If two ions, 1 and 2, exist throughout the volume of the wind, then their relative optical depths depend on the run of ionization fractions $q(r)$, the abundance of each element A , the relative oscillator strengths of the transition f , and their wavelengths:

$$\frac{\tau_1}{\tau_2} = \frac{q_1(r) A_1 f_1 \lambda_1}{q_2(r) A_2 f_2 \lambda_2} . \quad (2)$$

If their ionization fractions are constant throughout the wind at their photospheric values, then the relative strengths of the wind features due to N v, Si iv, and C iv are presented in Table 5. Based on this simple analysis, we would not expect detectable wind features from either Si iv or C iv.

Effects other than abundance may be at work. Bouret et al. (2013) observed 22 main-sequence O-type stars in the SMC with the Cosmic Origins Spectrograph (COS) aboard *HST*. Several of these stars have effective temperatures and surface gravities similar to those of vZ 1128, but they are considerably more metal rich, with abundances roughly a factor of five below solar. In particular, their atmospheres are not enhanced in nitrogen. Nevertheless, they exhibit the pattern seen in vZ 1128: broad P Cygni profiles in both components of the N v $\lambda 1240$ doublet, but no other FUV wind features. As an example, Fig. 8 presents the N v $\lambda 1240$, Si iv $\lambda 1397$, and C iv $\lambda 1550$ features of the star ELS 31 ($T_{\text{eff}} = 37,200 \text{ K}$, $\log g = 4.00$) in the star cluster NGC 346 (Evans et al. 2006). Because the star has a C/N ratio of 4.0, Eq. 2 predicts that the optical depth of wind features in the C iv doublet would be 2.5 times those in N v, yet no blue-shifted C iv absorption is seen.

6 DISCUSSION

In Fig. 9, the measured abundances of vZ 1128 (solid symbols) are compared with those of the sun (short horizon-

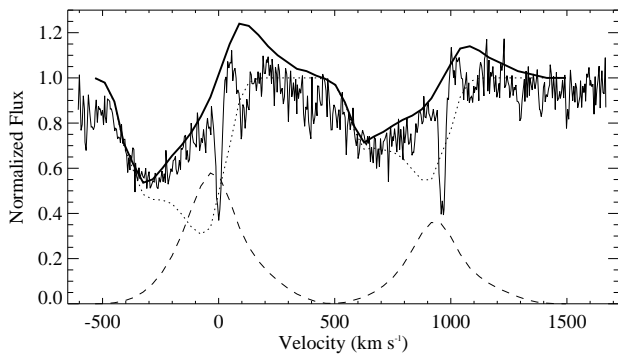


Figure 7. N v $\lambda 1240$ doublet, which shows a P Cygni profile. The data are overplotted by the wind model described in the text (thick solid line). Also shown are the transmitted (dotted line) and scattered (dashed line) components of the model profile. The spectrum is plotted in the stellar rest frame and centered on the blue component of the doublet. Photospheric and interstellar nitrogen absorption features are not included in the model.

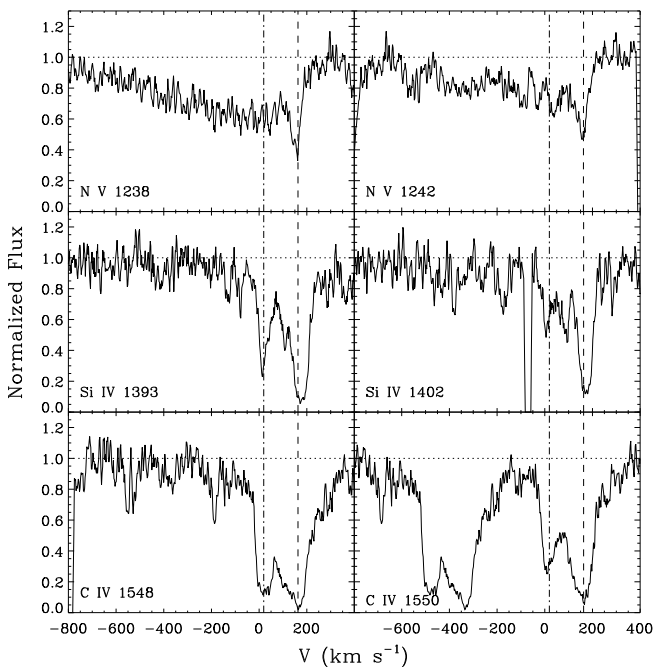


Figure 8. Normalized profiles of resonance doublets in the COS spectrum of ELS 31 in the SMC cluster NGC 346, plotted in a heliocentric reference frame. The dotted line corresponds to the normalized continuum. The vertical dashed lines indicate the radial velocity of the star (162.9 km s^{-1}). The vertical dot-dashed lines indicate the central velocity of the interstellar features due to our galaxy (19.2 km s^{-1}). Like $\nu Z 1128$, the star exhibits P Cygni profiles only in the N v $\lambda 1240$ doublet.

tal lines; Asplund et al. 2009) and M3 (rectangles). The He abundance is measured on the horizontal branch (HB; Behr 2003). Metal abundances are from red-giant-branch (RGB) stars: the C and N abundances are from Smith et al. (1996), and the O, Al, Si, Fe, and Ni values are from Sneden et al. (2004). The vertical extent of each rectangle represents the star-to-star scatter in the measured abundance ($\pm 1\sigma$ about

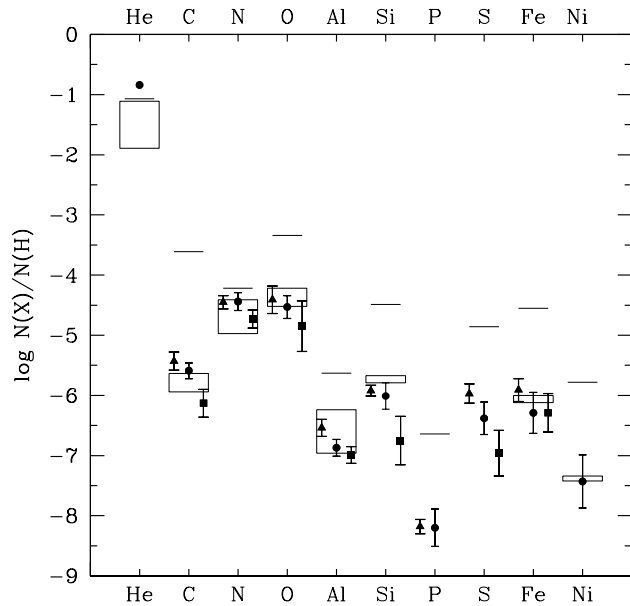


Figure 9. Comparison of the abundances derived for $\nu Z 1128$ (filled symbols) with those of the solar photosphere (short horizontal lines) and of HB and RGB stars in M3 (rectangles). Stellar abundances derived without an additional source of line broadening are plotted as circles, those allowing for stellar rotation are plotted as triangles, and those allowing for microturbulence are plotted as squares.

the mean). Beginning with the most massive elements, we see that the abundances of Si, Fe, and Ni are nearly constant along the RGB. The scatter is much larger for CNO and Al, reflecting well-known abundance variations in globular-cluster giants (Kraft 1994). For all of these elements, the measured abundances of $\nu Z 1128$ are consistent with those of the RGB stars.

6.1 Helium Abundance

The He abundance of $\nu Z 1128$ is nearly twice the solar value ($\log N(\text{He})/N(\text{H}) = -1.07$; Asplund et al. 2009). While RGB stars are too cool to show helium absorption, HB stars with $9000 \text{ K} < T_{\text{eff}} < 11,200 \text{ K}$ are hot enough to excite optical He I lines but not so hot that gravitational settling reduces the surface helium abundance. Behr (2003) derived helium abundances for five HB stars in M3. Though their uncertainties are large, they average $\log N(\text{He})/N(\text{H}) = -1.50 \pm 0.39$, roughly a third of the solar value. If this result is borne out, then $\nu Z 1128$ would be enhanced in He relative to the cluster mean.

6.2 CNO Abundances

Smith et al. (1996) investigated the variations in CNO abundance of stars on the RGB of M3 and M13, which have similar metallicities. We plot their data in Fig. 10, with the following changes: we express abundances in terms of $\log N(X)/N(\text{H})$ rather than $[X/\text{Fe}]$, and we use oxygen abundances from Sneden et al. (2004) where available. The

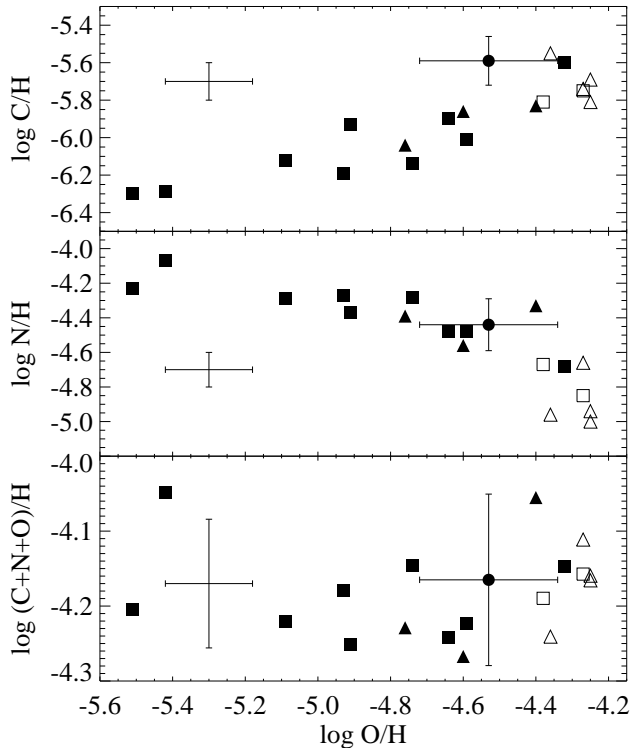


Figure 10. Abundance ratios of red giants in the globular clusters M3 (triangles) and M13 (squares). CN-poor stars are plotted as solid symbols, CN-poor stars as open symbols. The abundances of C and O are correlated, N and O are anticorrelated, and the total abundance of (C+N+O) is essentially constant, consistent with the products of CNO-cycle processing. The abundance ratios of *vZ 1128* in M3 (circles) are consistent with the patterns seen in the RGB stars.

results of Smith et al. (1996) are reproduced: the abundances of C and O are correlated, the N abundance is anticorrelated with both C and O, and the total abundance C+N+O is nearly constant. These patterns can be explained as the result of CNO-cycle hydrogen burning, which converts carbon (rapidly) and oxygen (slowly) into nitrogen, but leaves the total C+N+O abundance unchanged. Comparing abundances derived from non-LTE models of a sdO-type star observed in the FUV with those derived from LTE models of K-type giants observed in the optical may not be appropriate; nevertheless, we have added *vZ 1128* to Fig. 10. Though its carbon abundance is a bit high, the star’s CNO abundances follow the trends seen in the cluster’s RGB stars remarkably well. (Note that we plot the *vZ 1128* abundances derived without an additional source of line broadening; these values are plotted as circles in Fig. 9.)

6.3 Iron Abundance

Spectroscopic analyses of hot post-AGB field stars at high Galactic latitudes (McCausland et al. 1992, Napiwotzki et al. 1994) reveal that their Fe abundances are quite low, on the order of $[\text{Fe}/\text{H}] = -2.0$. Moehler et al. (1998) found that, among hot post-AGB stars in globular clusters, Barnard 29 in M13 and ROA 5701 in ω Cen exhibit iron depletions of ~ 0.5 dex relative to the cluster

RGB. Changes in iron abundance due to nucleosynthesis are not expected in low-mass stars, so these results are puzzling. Using new optical data, Thompson et al. (2007) have recently derived iron abundances for both Barnard 29 and ROA 5701 that are consistent with the cluster mean. We obtain a similar result for *vZ 1128* (Fig. 9).

Dixon et al. (1994) quote a metallicity for *vZ 1128* of $[\text{M}/\text{H}] = -3.5 \pm 1.5$. In their analysis, the authors compared the shape of the star’s far-UV spectrum (900–1850 Å) with those of synthetic spectra computed by Kurucz (1992), which assume solar abundance ratios. The authors reported that models with abundances $[-2.5]$, $[-3.0]$, and $[-3.5]$ all fell within the 2σ error ellipse of the best-fit model. While the grid of models with abundance $[-2.0]$ did not extend to temperatures above 32,000 K, they estimated that models with this abundance would also have fallen within the error ellipse. No models with abundance of $[-1.5]$ or higher fell within the error ellipse. In effect, Dixon et al. (1994) were able to set only an upper limit of $[\text{M}/\text{H}] = -1.5$ on the star’s metallicity, a value consistent with our iron abundance, which is derived from fits to individual spectral features.

6.4 Stellar Evolution

A star’s atmospheric abundances are modified by its post-main sequence evolution. According to stellar evolutionary theory (Iben & Renzini 1983), a star’s arrival on the red giant branch is accompanied by a deepening of its convective envelope, which brings to the surface the ashes of hydrogen burning via the CNO cycle. As a result of this process, known as first dredge-up, we expect to see a doubling of the surface ^{14}N abundance, a reduction in the ^{12}C abundance of about 30%, and practically no change in the abundance of ^{16}O .

No further mixing on the RGB is predicted by theory, but observations of low-mass red giants in both clusters and the field (e.g., Gratton et al. 2000) suggest that some form of mixing continues to bring CNO-processed material to the surface. The carbon abundance continues to fall, and the nitrogen abundance to rise (corresponding to a migration from right to left in Fig. 10) as a star ascends the RGB (Smith 2002).

No mixing is expected to occur on the horizontal branch. A second period of dredge-up can occur at the base of the AGB, but only in stars more massive than those seen in globular clusters today. Third dredge-up occurs near the tip of the AGB, as stars experience thermal pulses in their helium-burning shells. Third dredge-up brings ^{12}C and s-process isotopes produced by the burning of helium into the convective envelope. As a result, the atmospheric C/O ratio quickly exceeds unity (Van Winckel 2003). We expect *vZ 1128* to exhibit the effects of first dredge-up, any extra mixing that took place on the RGB, and third dredge-up, if it occurred.

The stellar temperature and luminosity derived by Dixon et al. (1994) place *vZ 1128* on the $0.546 M_{\odot}$ post-AGB evolutionary track of Schönberner (1983). This track traces the evolution of a star that leaves the AGB before the onset of thermal pulsing. Such objects are known as post-early AGB (post-EAGB) stars. This scenario is consistent with the abundance pattern seen in the atmosphere

of vZ 1128: its carbon abundance is not enhanced, nor are any s-process elements detected. We conclude that the star has not undergone third dredge-up. Indeed, it appears that no significant changes in its atmospheric composition have occurred since the star left the RGB.

We should not be surprised that vZ 1128 is a post-EAGB star. Post-AGB stars evolve quickly, remaining luminous for only 10^3 – 10^4 years, while post-EAGB stars remain luminous for 10^4 – 10^5 years (Schönberner 1981, 1983). Of the roughly one dozen UV-bright stars in globular clusters whose spectra have been analyzed to date (see Moehler 2010 for a review), only two show the enhanced carbon abundance expected of a star that evolved to the tip of the AGB. The first, K648 in M15 (Rauch et al. 2002), hosts a planetary nebula. The second, ZNG 1 in M5, lacks a nebula, and its high helium abundance and high rotational velocity suggest an unusual evolutionary history (Dixon et al. 2004). The dearth of carbon-rich post-AGB stars in galactic globular clusters is consistent with the short lifetimes of these rare objects.

7 CONCLUSIONS

We have analyzed *FUSE*, STIS, and Keck spectra of the UV-bright star vZ 1128 in M3. We determine the star’s atmospheric parameters by fitting the hydrogen and helium lines in its Keck spectrum with non-LTE H-He models. The star’s *FUSE* and STIS spectra show photospheric absorption from C, N, O, Al, Si, P, S, Fe, and Ni, but no absorption from elements beyond the iron peak. We determine the abundance of each element by comparing its observed lines to a grid of synthetic spectra. Additional broadening is required to reproduce the line cores, though we cannot distinguish between stellar rotation or microturbulence as the source. Modeling the star’s nitrogen lines proved particularly challenging: Reproducing three N III emission features in the star’s HIRES spectrum required the use of a more sophisticated model atom. Obtaining reasonable nitrogen abundances from a pair of N IV absorption features in the star’s *FUSE* spectrum required the use of larger oscillator strengths. Finally, both components of the N V λ 1240 doublet in the star’s STIS spectrum exhibit P Cygni profiles, indicating a weak stellar wind, though no other wind features are seen. The star’s photospheric abundances appear to have changed little since it left the RGB. Its C, N, O, Al, Si, Fe, and Ni abundances are consistent with those of cluster RGB stars; in particular, the relative abundances of C, N, and O follow the trends seen on the cluster RGB. Its low C abundance suggests that the star left the AGB before the onset of third dredge-up, making vZ 1128 a post-early AGB star.

ACKNOWLEDGMENTS

The authors wish to thank L. M. Torres and J. M. Rivera for their assistance with spectral-line fitting, J. C. Howk for help with the STIS data, and I. Hubeny and T. Lanz for providing their stellar atmosphere and spectral synthesis codes. This research has made use of NASA’s Astrophysics Data System Bibliographic Services and the SIMBAD database, operated at CDS, Strasbourg, France. It has also made use of the

Keck Observatory Archive (KOA), which is operated by the W. M. Keck Observatory and the NASA Exoplanet Science Institute (NExScI), under contract with NASA. The STIS data presented in this paper were obtained from the Mikulski Archive for Space Telescopes (MAST). STScI is operated by the Association of Universities for Research in Astronomy, Inc., under NASA contract NAS5-26555. IDL is a registered trademark of Exelis Visual Information Solutions, Inc., for its Interactive Data Language software. This work was supported by NASA grant NAS5-32985 to the Johns Hopkins University. P.C. is supported by the Canadian Space Agency under a contract with NRC Herzberg Astronomy and Astrophysics. L. M. Torres and J. M. Rivera were supported by NASA contract NNG04D58G.

REFERENCES

- Allard N., Artru M.-C., Lanz T., Le Dourneuf M., 1990, *A&AS*, 84, 563
 Allard N., Le Dourneuf M., Artru M.-C., Lanz T., 1991, *A&AS*, 91, 399
 Asplund M., Grevesse N., Sauval A. J., Scott P., 2009, *ARA&A*, 47, 481
 Behr B. B., 2003, *ApJS*, 149, 67
 Bostroem K., Proffitt C., 2011, *STIS Data Handbook*, vol. 6.0. STScI, Baltimore, MD
 Bouret J.-C., Lanz T., Martins F., Marcolino W. L. F., Hillier D. J., Depagne E., Hubeny I., 2013, *A&A*, 555, A1
 Buzzoni A., Cacciari C., Fusi-Pecchi F., Buonanno R., Corsi C. E., 1992, *A&A*, 254, 110
 Danly L., Lockman F. J., Meade M. R., Savage B. D., 1992, *ApJS*, 81, 125
 de Boer K. S., 1985, *A&A*, 142, 321
 de Boer K. S., Savage B. D., 1984, *A&A*, 136, L7
 Dixon W. V., Brown T. M., Landsman W. B., 2004, *ApJ*, 600, L43
 Dixon W. V., Davidsen A. F., Ferguson H. C., 1994, *AJ*, 107, 1388
 Dixon W. V., Sahnou D. J., Barrett P. E., Civeit T., Dupuis J., Fullerton A. W., Godard B., Hsu J.-C., Kaiser M. E., Kruk J. W., Lacour S., Lindler D. J., Massa D., Robinson R. D., Romelfanger M. L., Sonnentrucker P., 2007, *PASP*, 119, 527
 Evans C. J., Lennon D. J., Smartt S. J., Trundle C., 2006, *A&A*, 456, 623
 Garrison R. F., Albert C. E., 1986, *ApJ*, 300, L69
 Gratton R. G., Sneden C., Carretta E., Bragaglia A., 2000, *A&A*, 354, 169
 Guerrero M. A., De Marco O., 2013, *A&A*, 553, A126
 Harris W. E., 1996, *AJ*, 112, 1487
 Howk J. C., Sembach K. R., Savage B. D., 2003, *ApJ*, 586, 249
 Howk J. C., Sembach K. R., Savage B. D., 2006, *ApJ*, 637, 333
 Hubeny I., Lanz T., 1995, *ApJ*, 439, 875
 Iben Jr. I., Renzini A., 1983, *ARA&A*, 21, 271
 Kimble R. A., et al., 1998, *ApJ*, 492, L83
 Kraft R. P., 1994, *PASP*, 106, 553
 Kurucz R. L., 1992, in Barbuy B., Renzini A., eds, *The Stellar Populations of Galaxies Vol. 149 of IAU Symposium, Model Atmospheres for Population Synthesis*. p. 225

- Kurucz R. L., Bell B., 1995, Atomic Line Data Kurucz CD-ROM No. 23. Cambridge, Mass.: Smithsonian Astrophysical Observatory, 23
- Lamers H. J. G. L. M., Cerruti-Sola M., Perinotto M., 1987, *ApJ*, 314, 726
- Lanz T., Hubeny I., 2003, *ApJS*, 146, 417
- Lanz T., Hubeny I., 2007, *ApJS*, 169, 83
- Massa D., Fullerton A. W., Sonneborn G., Hutchings J. B., 2003, *ApJ*, 586, 996
- Massa D., Prinja R. K., Fullerton A. W., 1995, *ApJ*, 452, 842
- McCausland R. J. H., Conlon E. S., Dufton P. L., Keenan F. P., 1992, *ApJ*, 394, 298
- Moehler S., 2010, *MmSAI*, 81, 838
- Moehler S., Heber U., Lemke M., Napiwotzki R., 1998, *A&A*, 339, 537
- Moos H. W., et al., 2000, *ApJ*, 538, L1
- Napiwotzki R., Heber U., Koeppen J., 1994, *A&A*, 292, 239
- Pauldrach A., Puls J., Kudritzki R. P., Mendez R. H., Heap S. R., 1988, *A&A*, 207, 123
- Rauch T., Heber U., Werner K., 2002, *A&A*, 381, 1007
- Sahnou D. J., et al., 2000, *ApJ*, 538, L7
- Schönberner D., 1981, *A&A*, 103, 119
- Schönberner D., 1983, *ApJ*, 272, 708
- Smith G. H., 2002, *PASP*, 114, 1097
- Smith G. H., Shetrone M. D., Bell R. A., Churchill C. W., Briley M. M., 1996, *AJ*, 112, 1511
- Snedden C., Kraft R. P., Guhathakurta P., Peterson R. C., Fulbright J. P., 2004, *AJ*, 127, 2162
- Strom S. E., Strom K. M., 1970, *ApJ*, 159, 195
- Strom S. E., Strom K. M., Rood R. T., Iben Jr. I., 1970, *A&A*, 8, 243
- Thompson H. M. A., Keenan F. P., Dufton P. L., Ryans R. S. I., Smoker J. V., Lambert D. L., Zijlstra A. A., 2007, *MNRAS*, 378, 1619
- Tully J. A., Seaton M. J., Berrington K. A., 1990, *Journal of Physics B Atomic Molecular Physics*, 23, 3811
- Van Winckel H., 2003, *ARA&A*, 41, 391
- von Zeipel H., 1908, *Annales de l'Observatoire de Paris*, 25, F1
- Wiese W. L., Fuhr J. R., Deters T. M., 1996, Atomic transition probabilities of carbon, nitrogen, and oxygen: a critical data compilation. American Institute of Physics, Woodbury, NY
- Woodgate B. E., et al., 1998, *PASP*, 110, 1183